Liouvillian Spectral Transition in Noisy Quantum Many-Body Scars

Jin-Lou Ma,[1,*] Zexian Guo,[1,*] Yu Gao,[1] Zlatko Papić,[2,†] and Lei Ying[1,†]
[1]*School of Physics and Zhejiang Key Laboratory of Micro-nano Quantum Chips and Quantum Control, Zhejiang University, Hangzhou 310027, China*
[2]*School of Physics and Astronomy, University of Leeds, Leeds LS2 9JT, United Kingdom*

(Received 21 April 2025; revised 10 August 2025; accepted 7 October 2025; published 29 October 2025)

Understanding the behavior of quantum many-body systems under decoherence is essential for developing robust quantum technologies. Here, we examine the fate of weak ergodicity breaking in systems hosting quantum many-body scars when subject to local pure dephasing—an experimentally relevant form of environmental noise. Focusing on a large class of models with an approximate su(2)-structured scar subspace, we show that scarred eigenmodes of the Liouvillian exhibit a transition reminiscent of spontaneous $\mathbb{PT}$-symmetry breaking as the dephasing strength increases. Unlike previously studied non-Hermitian mechanisms, this transition arises from a distinct quantum jump effect. Remarkably, in platforms such as the XY spin ladder and PXP model of Rydberg atom arrays, the critical dephasing rate shows only weak dependence on the system size, revealing an unexpected robustness of scarred dynamics in noisy environments.

DOI: 10.1103/4my3-vk6c

Introduction—Recent advances in quantum simulations [1–5] have opened a window to studying thermalization in isolated quantum many-body systems [6–10]. Many such systems are now understood to host atypical nonthermalizing eigenstates known as quantum many-body scars (QMBSs) [11–13]. QMBSs are ubiquitous in many physical systems, including Rydberg atom arrays [14–28], the Heisenberg-type spin systems [29–32], ultracold atoms in tilted optical lattices [33–38], superconducting circuits [39,40], and many others [41–59]. The unique properties of QMBSs are also of interest in quantum information processing [60–62]; e.g., they have been used to prepare Greenberger-Horne-Zeilinger states [63].

The existing platforms for quantum simulation, however, are prone to decoherence caused by the surrounding environment. The decoherence—particularly pure dephasing—can significantly impact individual qubits [64], limiting their dephasing time to around 20 μs in current state-of-the-art superconducting platforms [65]. While dissipation was studied in kinetically constrained models [66,67] and time crystals [68–71], its impact on the robustness of QMBS states remains poorly understood [72–74]. Previous studies of QMBSs to perturbations in closed systems [75,76] suggest that they might quickly thermalize in the presence of noise. Moreover, while Ref. [72] recently demonstrated a construction for embedding QMBS into decoherence-free subspaces, a comprehensive understanding of realistic decoherence effects, such as pure dephasing, remains elusive.

In this Letter, we consider a large class of QMBS models coupled to the environment via local pure dephasing γ on each site. We focus on models with a so-called restricted su(2) spectrum generating algebra [77–80], which includes experimentally realized QMBSs in several platforms [14,37,39,81]. In the absence of dephasing, these QMBS eigenstates distribute with nearly equal energy spacings and the system exhibits long-lived coherent dynamics when prepared in special initial states. As the dephasing increases beyond a critical value $\gamma_\star$, the thermal bulk of the spectrum undergoes a spontaneous Liouvillian $\mathbb{PT}$-symmetry (LPTS) breaking transition [82]. This occurs rapidly, as the critical dephasing is inversely proportional to the square of the Liouvillian eigenvalue density [82] and hence exponentially small in system size, $\gamma_\star \sim \exp(-L)$. By contrast, we find that QMBS eigenvalues undergo a distinct spectral transition at $\gamma_\star^{\mathrm{S}}$, which scales polynomially with system size, $\gamma_\star^{\mathrm{S}} \sim L^{-1}$. This difference in scaling has a striking manifestation for the robustness of QMBS signatures under dissipative dynamics. We identify the origin of this phenomenon in the quantum jumper effect beyond previously considered non-Hermitian mechanisms [83,84]. We illustrate our conclusions using an experimentally relevant model of superconducing qubits from Refs. [39,81], while

---

[*] These authors contributed equally to this work.
[†] Contact author: z.papic@leeds.ac.uk
[‡] Contact author: leiying@zju.edu.cn

in End Matter we provide further evidence for the PXP model of Rydberg atom arrays [14].

Creutz ladder (CL) model—We consider a paradigmatic QMBS model describing superconducting qubits in a Creutz ladder configuration [39,85]. A variant of this model was used to experimentally demonstrate QMBS-enabled tunability of entanglement in the presence of disorder [81]. The total Hamiltonian, $\hat{H} = \hat{H}_{\mathrm{CL}} = \hat{H}_{\mathrm{h},1} + \hat{H}_{\mathrm{h},2} + \hat{H}_{\mathrm{v}} + \hat{H}_{\mathrm{x}}$, is a sum of Hamiltonians $\hat{H}_{\mathrm{h},\alpha}$ for each of the two horizontal legs $\alpha \in \{1, 2\}$ of the ladder, the vertical coupling between them, $\hat{H}_{\mathrm{v}}$, and the cross-coupling $\hat{H}_{\mathrm{x}}$ present in experiment [39,81]:

$$\begin{aligned}\hat{H}_{\mathrm{h},\alpha} &= J_{\mathrm{h}} \sum_j \left[(-1)^{j+\alpha} \hat{\sigma}^{+}_{j,\alpha} \hat{\sigma}^{-}_{j+1,\alpha} + \mathrm{H.c.}\right],\\ \hat{H}_{\mathrm{v}} &= J \sum_j \left(\hat{\sigma}^{+}_{j,1} \hat{\sigma}^{-}_{j,2} + \mathrm{H.c.}\right),\\ \hat{H}_{\mathrm{x}} &= \sum_j J_{\mathrm{x},j} \left(\hat{\sigma}^{+}_{j,1} \hat{\sigma}^{-}_{j+1,2} + \hat{\sigma}^{+}_{j,2} \hat{\sigma}^{-}_{j+1,1} + \mathrm{H.c.}\right), \qquad (1)\end{aligned}$$

where $\hat{\sigma}^{\pm}_{j,\alpha}$ is the standard raising (lowering) spin-1/2 operator for jth spin in layer α. The ladder contains $L = 2N$ spins in total. We use "$\uparrow, \downarrow$" to denote the standard spin basis states of a single site, assume open boundary conditions, and set $J = 1$ as the overall energy scale. Note that the cross-coupling $J_{\mathrm{x},j}$ can be site dependent or even random.

When $J_{\mathrm{x},j} = 0$, the CL model hosts exact QMBS eigenstates, which are simply the Dicke states of a collective spin of magnitude N:

$$\hat{S}_0 = \sum_{j=1}^{N} (|{\Uparrow}\rangle\langle{\Downarrow}|_j + |{\Downarrow}\rangle\langle{\Uparrow}|_j). \qquad (2)$$

This operator is defined in the basis $|{\Uparrow}\rangle \equiv |{\substack{\uparrow\\ \downarrow}}\rangle$, $|{\Downarrow}\rangle \equiv |{\substack{\downarrow\\ \uparrow}}\rangle$; see Supplemental Material (SM) for details [86]. In the limit $J_{\mathrm{x},j} = 0$, the CL Hamiltonian splits into a direct sum of scar and thermal subspaces, $\hat{H} = \hat{S}_0 \oplus \hat{T}$, and the product state $|\Pi\rangle = |{\Uparrow\Uparrow\Uparrow}\cdots\rangle$ has no component outside $\hat{S}_0$. Thus, $|\Pi\rangle$ undergoes perfect revivals when $J_{\mathrm{x},j} = 0$, corresponding to the free precession of the collective spin. On the other hand, when $J_{\mathrm{x},j} \neq 0$, the QMBS eigenstates are only approximately given by the Dicke states, and a small coupling $\hat{V}$ then connects the scar and thermal subspaces, $\hat{H} = \hat{S}_0 \oplus \hat{T} + \hat{V}$. This causes the revivals to acquire a decaying envelope, as observed in experiment [81].

Liouvillian spectral transition—We now consider each spin to have local decoherence to a bath. Under the Markov approximation, such a system is generally described by a Liouville superoperator [87]. Here, we focus on pure dephasing, with the corresponding superoperator

$$\mathcal{L} = -i(\hat{H} \otimes \hat{I} - \hat{I} \otimes \hat{H}^{*}) + \gamma \mathcal{D}, \qquad (3)$$

where γ is the pure dephasing rate, the dissipator is $\mathcal{D} = \mathcal{D}' - \sum_j \hat{I}_j \otimes \hat{I}_j$ with $\mathcal{D}' = \sum_j \hat{\sigma}^z_j \otimes \hat{\sigma}^z_j$. The operator $|E_n\rangle\langle E_m|$ in $\mathcal{L}$ has a vector representation given by $|E_n\rangle \otimes |E_m\rangle$ [87], where $|E_n\rangle$ and $|E_m\rangle$ are eigenstates of the entire Hamiltonian with $n, m = 1, 2, \ldots, D$ and D is the Hilbert space dimension. The kth eigenvalue and eigenmode of the Liouville superoperator in Eq. (3) are denoted by λ_k and $|\lambda_k\rangle\rangle$, respectively, with $k = 1, 2, \ldots, D^2$. To understand the spectral properties of $\mathcal{L}$, we perform a transformation $\mathcal{L}' = \mathcal{L} + \gamma(\mathrm{Tr}(\mathcal{D})/\mathrm{Tr}(\mathcal{I}))\mathcal{I}$, with $\mathcal{I} = \hat{I} \otimes \hat{I}$, which makes the Liouvillian spectrum traceless, i.e., sets the average of $\mathrm{Re}(\lambda'_k)$ to zero [82].

For an isolated system with cross couplings turned off, $\gamma = J_{\mathrm{x},j} = 0$, the Liouvillian of scar subspace is $\mathcal{S}_0 = -i(\hat{S}_0 \otimes \hat{I} - \hat{I} \otimes \hat{S}_0)$. The spectrum of $\mathcal{S}_0$ is purely imaginary and the eigenmodes are tensor products of previously mentioned Dicke states for Eq. (2):

$$|\lambda^{(0)}_{(l,s)}\rangle\rangle = |E^{\mathrm{S}}_{l+s}\rangle \otimes |E^{\mathrm{S}}_{s}\rangle, \quad \lambda^{(0)}_{(l,s)} = i(E^{\mathrm{S}}_{l+s} - E^{\mathrm{S}}_{s}) = 2il, \qquad (4)$$

where E^{S} and $|E^{\mathrm{S}}\rangle$ represent the eigenenergy and eigenstate of $\hat{S}_0$, respectively. For later convenience, we use indices $l = -N, -N+1, \ldots, N$ and $s = 0, 1, \ldots, N - |l|$ to label the scar eigenmodes. For small γ, we will use the overlap with states in Eq. (4) to identify QMBS eigenmodes of the full Liouvillian. For stronger dephasings, we identify QMBS states by following smooth changes of the spectrum as γ is slowly varied.

The Liouvillian spectra of the CL model in Eq. (1) with $J_{\mathrm{h}} = 0.66$, $J_{\mathrm{x},j} = 0.1$ are presented in Fig. 1. We show illustrative examples of the spectra before (a) and after (b) the spectral transition. The QMBS eigenmodes (red and blue circles) are distinguished by their enhanced overlap with the state $|\rho_{\Pi}\rangle\rangle = |\Pi\rangle \otimes |\Pi\rangle$, also shown in Fig. 1. These eigenvalues are furthermore distinguished by their symmetry quantum number $p = \pm 1$ under inversion, generated by $\prod_j (\hat{\sigma}^x_{j,1} \hat{\sigma}^x_{j,2}) \otimes (\hat{\sigma}^x_{j,1} \hat{\sigma}^x_{j,2})$. Before the spectral transition, Fig. 1(a), the identified QMBS eigenvalues cluster on the imaginary axis, unlike the thermal eigenvalues (yellow and gray circles). After the transition [Fig. 1(b)], the same QMBS eigenvalues exhibit a qualitatively different distribution pattern in the form of a sparse diamond grid across the complex plane. For a system of N qubits per leg, the QMBS eigenvalues undergoing this transition are layers $l = -N, 2 - N, \ldots, N - 2, N$ in Eq. (4). Thus, they alternate between inversion symmetry sectors given by $p = (-1)^l$.

The change in the distribution of eigenvalues in the complex plane in Fig. 1 is reminiscent of an LPTS breaking transition [82]. However, most of the thermal eigenvalues have already undergone LPTS breaking at $\gamma = 0.0005$ in Fig. 1(a), suggesting that QMBS eigenvalues undergo a

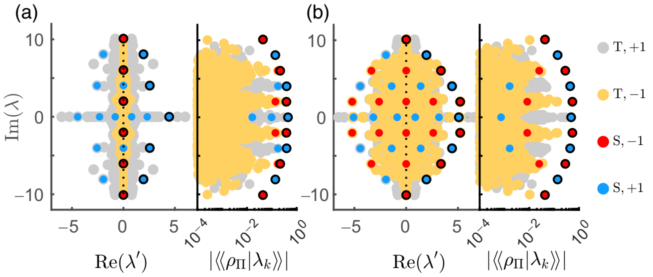

FIG. 1. (a),(b) The Liouvillian spectra (left panel) and the overlap with $|\rho_\Pi\rangle\rangle$ (right panel) of the CL model, Eq. (1), for dephasing strengths $\gamma = 0.0005$ (a) and 0.02 (b). We plot the imaginary part of Liouvillian eigenvalues λ_k against the real part of shifted eigenvalues λ'_k. Red and blue dots represent scar (S) eigenvalues, while yellow and gray ones represent thermal (T) eigenvalues, labeled according to their inversion symmetry quantum number, $p = \pm 1$. Open black circles represent scar states corresponding to local maxima in the overlaps (right panels). The scar eigenvalues in "S, −1" sector undergo a spectral transition as γ increases, while those in "S, +1" do not [compare red dots in panel (a) with (b)]. The data is obtained by exact diagonalization for couplings $J_\mathrm{h} = 0.66$, $J_{\mathrm{x},j} = 0.1$, system size $L = 10$ with open boundary conditions.

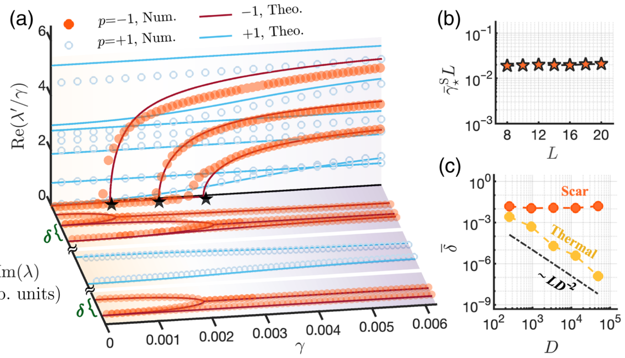

FIG. 2. (a) The evolution of the Liouvillian spectrum in the CL model, Eq. (1), with couplings $J_\mathrm{h} = 0.66$, $J_{\mathrm{x},j} = 0.1$ and system size $L = 10$ with open boundary conditions. We plot $\mathrm{Im}(\lambda)$ and $\mathrm{Re}(\lambda'/\gamma)$, as the dephasing rate γ is varied. For improved visualization, the imaginary eigenvalues have been offset within a small window. Analytical prediction of perturbation theory (lines) are in good agreement with the numerical data, in particular for the spectral transition points $\gamma_\star^{\mathrm{S}(1,2,3)}$ (black stars). (b) The average spectral transition point, $\bar{\gamma}_\star^S L$, as a function of the system size L obtained in perturbation theory. (c) The average spacing $\bar{\delta}$ between the scarred and thermal eigenenergies in the dephasing-free case, plotted as a function of the Hilbert space dimension D.

distinct transition. Moreover, it is only a subset of those eigenvalues belonging to "S, −1" sector in Fig. 1 that undergo such a transition. Below we show that the spectral transition of these QMBS eigenvalues leaves an imprint on the dissipative dynamics, and we develop their perturbative description to reveal the distinction from an LPTS breaking transition of thermal eigenvalues.

Liouvillian perturbation theory—To examine the spectral transition in Fig. 1 more quantitatively, we study the spectra as we sweep the dephasing rate γ in Fig. 2(a). At weak dephasing, several eigenvalues with inversion symmetry $p = -1$ remain stationary along the real axis, while moving along the imaginary one. As γ increases, pairs of these eigenvalues collide on the imaginary axis and abruptly bifurcate into two branches at specific dephasing rates $\gamma_\star^{\mathrm{S}(1,2,3)}$ along the real axis [for clarity, only the positive branch is shown in Fig. 2(a)].

To understand the spectral evolution in Fig. 2(a), we have developed a Liouvillian degenerate perturbation theory valid for small γ. If we neglect the coupling between the bath and the thermal subsystem, the effective Liouvillian for the scar subspace is $\mathcal{L}_\mathcal{S} \approx \mathcal{S}_0 + \mathcal{E} + \gamma_\mathrm{eff}\mathcal{D}'$, where $\mathcal{E} = -i(\hat{\Sigma} \otimes \hat{I} - \hat{I} \otimes \hat{\Sigma})$ is the self-energy superoperator that includes the effect of thermal bulk [86]. The effective dephasing $\gamma_\mathrm{eff} = 2\gamma$ accounts for the magnitude of collective spin being half the system size, $N = L/2$.

In the regime $\|\mathcal{E} + \gamma_\mathrm{eff}\mathcal{D}'\| \ll \|\mathcal{S}_0\|$, the traceless Liouvillian eigenvalues for the lth layer are modified with respect to Eq. (4) into $\lambda'_{(l,s)} \approx \lambda^{(0)}_{(l,s)} + \lambda^{(1)}_{(l,s)}$, where the first-order corrections $\lambda^{(1)}_{(l,s)}$ are obtained by diagonalizing the projection of $(\mathcal{E} + \gamma_\mathrm{eff}\mathcal{D}')$ to the degenerate subspace of the lth layer. The projected matrix consists of an imaginary diagonal matrix $\mathcal{E}_l$ and a real shift matrix $\mathcal{D}'_l$:

$$\mathcal{E}_l = i \times \mathrm{Diag}\left[\Sigma_{(l,0)}, \Sigma_{(l,1)}, \ldots, \Sigma_{(l,N-|l|)}\right],$$

$$\mathcal{D}'_l = \sum_{s=0}^{N-|l|-1} d_{(l,s)}\left[|\lambda^{(0)}_{(l,s)}\rangle\rangle\langle\langle\lambda^{(0)}_{(l,s+1)}| + \mathrm{H.c.}\right], \qquad (5)$$

with $\Sigma_{(l,s)} = \langle E_s^\mathrm{S}|\hat{\Sigma}|E_s^\mathrm{S}\rangle - \langle E_{s+l}^\mathrm{S}|\hat{\Sigma}|E_{s+l}^\mathrm{S}\rangle$ and $d_{(l,s)} = \sqrt{(s+1)(N-s)(|l|+s+1)(N-|l|-s)}/N$ [86]. By diagonalizing $(\mathcal{E}_l + \gamma_\mathrm{eff}\mathcal{D}'_l)$, we obtain the perturbed eigenvalues for the lth layer and plot them against the numerical results for the same parameters in Fig. 2(a).

The perturbation theory results in Fig. 2(a) compare well with the numerics for both the imaginary and the real parts of the Liouvillian spectrum. The analytical prediction of $\gamma_\star^{\mathrm{S}(1,2,3)}$ implies that the spectral transition in QMBS Liouvillian spectra originates from the competition between dissipation $\gamma_\mathrm{eff}\mathcal{D}'$ and self-energy $\mathcal{E}$. While different QMBS eigenvalues undergo bifurcations at generally different values of $\gamma_\star^{\mathrm{S}(1,2\ldots)}$, the mean value $\bar{\gamma}_\star^\mathrm{S}$ has a robust universal scaling with L and determines the dynamical signatures studied below. Hence, we estimate the spectral transition point for QMBS Liouvillian eigenvalues:

$$\bar{\gamma}_\star^\mathrm{S} \sim \|\mathcal{E}\| \times \|\mathcal{D}'\|^{-1} \sim L^{-1}, \qquad (6)$$

which follows from the operator norm of $\mathcal{D}'$ being extensive in system size, while $\|\mathcal{E}\|$ is independent of L [86]. This estimate, shown in Fig. 2(b), is consistent with Fig. 2(c), where we numerically extract the average spacing $\bar{\delta}$ for scar and thermal eigenvalues in the dephasing-free case ($\gamma = 0$) as a function of the Hilbert space dimension D. The typical spacing for thermal eigenvalues scales as $\bar{\delta} \sim LD^{-2}$, while the scar $\bar{\delta}^{\mathrm{S}}$ is nearly independent of D. Then, the heuristic estimate of the typical spectral transition point, $\bar{\gamma}_\star^{\mathrm{S}} \sim \bar{\delta}^{\mathrm{S}} \|\mathcal{D}'\|^{-1}$, is in agreement with Eq. (6). This is in stark contrast with the exponential scaling $\bar{\gamma}_\star \sim D^{-2}$ of thermal eigenvalues [82]. Thus, the presence of QMBSs gives rise to spectral transition points that scale polynomially with system size and have robust dynamical signatures, as shown next.

Dynamical signatures—We demonstrate that weak dependence of $\bar{\gamma}_\star^{\mathrm{S}}$ on system size allows for QMBS signatures to persist in open-system dynamics defined by the evolution equation $\mathrm{d}|\rho(t)\rangle\rangle/\mathrm{d}t = \mathcal{L}|\rho(t)\rangle\rangle$ [87]. We integrate this equation starting from the initial state $|\rho_0\rangle\rangle = |\rho_\Pi\rangle\rangle$ and characterize subsequent time evolution by computing the fidelity and the density imbalance,

$$F(t) = \left| \sum_k \langle\langle \rho_0 | \lambda_k \rangle\rangle^2 e^{\lambda_k t} \right|, \quad I(t) = \frac{1}{L} \sum_j \langle\langle \mathcal{Z}_j \rangle\rangle_0 \langle\langle \mathcal{Z}_j \rangle\rangle_t, \tag{7}$$

where $\langle\langle \mathcal{Z}_j \rangle\rangle_t = \langle\langle \rho(t) | \hat{\sigma}_j^z \otimes \hat{\sigma}_j^z | \rho(t) \rangle\rangle$. As the fidelity dynamics directly corresponds to the Liouvillian spectrum, the variance of fidelity density at the first revival point $\ln(F_1)/L$, illustrated in Fig. 3(a), can reveal the Liouvillian spectrum transition. Furthermore, the imbalance dynamics takes the form of a damped oscillation [Fig. 3(b)], which we fit using $\bar{I}(t) = \exp(-\beta t)\cos(\omega t)$ to extract the decay rate β and revival frequency ω. In practice, we found it sufficient to fit the data up to the first revival period [86].

In Fig. 3(c), we plot $\ln(F_1)/L$ as a function of γL, while the extracted imbalance parameters (ω, β) are plotted in Fig. 3(d). Below the spectral transition point, both quantities are well converged and weakly depend on γL, which is indeed consistent with the spectral transition results in Fig. 1 and perturbation theory estimate in Eq. (6).

The dissipative dynamics in Fig. 3 highlight the difference between the QMBS systems where the su(2) spectrum generating algebra is exact ($J_{\mathrm{x},j} = 0$) versus only approximately obeyed ($J_{\mathrm{x},j} \neq 0$) within the scar subspace. In Figs. 3(c) and 3(d), we notice that the fidelity density and decay exponent β in the exact scar case both display power-law dependence on γL, in stark contrast with the plateau observed for $J_{\mathrm{x},j} \neq 0$. Thus, only approximate QMBSs undergo the spectral transition at a nonzero $\gamma_\star^{\mathrm{S}}$. This difference in behavior is due to the exact energy spacing at $J_{\mathrm{x},j} = 0$, which leads to degeneracies on the imaginary axis in Eq. (4). Hence, the Liouvillian eigenvalues of exact scars jump into the complex plane for any $\gamma \neq 0$, as confirmed in SM [86]. However, as the dephasing rate in Figs. 3(c) and 3(d) increases beyond $\bar{\gamma}_\star^{\mathrm{S}}$, the behaviors of approximate and exact scars become similar.

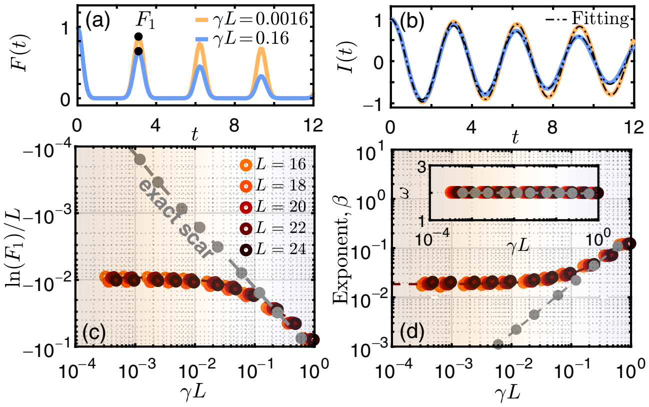

FIG. 3. The time evolution of the fidelity $F(t)$ (a) and the density imbalance $I(t)$ (b) for two dephasing rates at system size $L = 16$. The black circles in (a) represent the first peak of $F(t)$. The black dash-dotted lines in (b) represent the fit of $\bar{I}(t)$ (see text). The fidelity density at the first revival, $\ln(F_1)/L$ (c) and the decay coefficient β of density imbalance (d) for the CL model as a function of dephasing γ. For $\gamma < \bar{\gamma}_\star^{\mathrm{S}}$, both the fidelity density and imbalance decay are well-converged in system size, suggesting the robustness of scar signatures over a finite range of γL. By contrast, in the exact scar case with $J_{\mathrm{x},j} = 0$, the imbalance decay is highly sensitive to γ across the whole range. All data is for $J_{\mathrm{h}} = 0.66$, $J_{\mathrm{x},j} \in [0, 0.2]$ drawn from a uniform distribution. Parameters (β, ω) are obtained by fitting the imbalance dynamics over the time period [0, 3.2]. These results are obtained by TEBD algorithm based on ITensor library [88].

The nature of the spectral transition—In generic chaotic models (without QMBSs), the LPTS breaking can be understood from the symmetry classification developed in Ref. [89]. In particular, the existence of a superoperator $\mathcal{T}_-$ that obeys $\mathcal{T}_- \mathcal{L} \mathcal{T}_-^{-1} = -\mathcal{L}$ is responsible for the dihedral symmetry of the Liouvillian spectrum and $\mathbb{PT}$ breaking. At $\gamma = 0$, $|-(\lambda')^*\rangle\rangle$ and $|\lambda'\rangle\rangle$ represent the same state which lies on the imaginary axis. Beyond a certain γ, $\mathbb{PT}|\lambda'\rangle\rangle = |-(\lambda')^*\rangle\rangle$ continues to hold, but λ' and $-(\lambda')^*$ are no longer the same. Thus, after this critical point, pairs of degenerate eigenvalues move symmetrically away from the imaginary axis along the real axis, resulting in LPTS breaking [82].

One may wonder if a similar, symmetry-based argument can be applied to the QMBS spectral transition observed in Fig. 1 above. For the CL model, there indeed exists an analogous operator $\mathcal{T}_-$ (see SM [86] for its explicit form). However, the spectral transition in the CL model only occurs in inversion symmetry sector $p = -1(+1)$, corresponding to odd (even) N. See $N = 5$ case in Fig. 1. In contrast, the symmetry is already broken for infinitesimal γ in $p = +1(-1)$ sector, also correlating with even (odd) N. Thus, $\mathcal{T}_-$ by itself does not fully account for the observations in Fig. 1. As a more transparent example, in End Matter, we perform the same analysis for the PXP model of Rydberg atom arrays, finding a similar transition in its Liouvillian spectrum as a function of dephasing. The PXP model manifestly lacks the $\mathcal{T}_-$ symmetry [86], while it displays a spectral transition similar to Fig. 1 and robustness of QMBS dynamical signatures similar to Fig. 3. Thus, we conclude the QMBS spectral transition is not due to symmetry breaking, but due to the smallness of matrix elements connecting the QMBS subspace with thermal bulk of the spectrum.

Conclusions—By analyzing the Liouvillian spectra and dynamics in the presence of dephasing, we demonstrated that QMBSs can undergo a dissipative transition that resembles LPTS breaking. This behavior distinguishes approximate scar states from thermal states; the former exhibit a certain degree of robustness to a dephasing dissipation, reminiscent of their behavior under closed system dynamics when prepared in a thermal Gibbs state [90]. We note that quantum noise is crucial for observing the QMBS Liouvillian spectral transition phenomena as the latter do not persist under a non-Hermitian Hamiltonian approximation [86].

We supported our conclusions using the CL and PXP models realized in superconducting and Rydberg platforms. Notably, these two platforms allow for controlled dephasing noise [91,92] and can be used test our predictions for the imbalance dynamics by tuning the dephasing rate. Further numerical evidence for the Liouvillian spectral transition in the 1D tilted Fermi-Hubbard model [35], and ladder models with Hilbert space fragmentation [93] is presented in SM [86]. All of these models are described by the similar effective Hamiltonian $\hat{H} = \hat{S}_0 \oplus \hat{T} + \hat{V}$, suggesting broader applicability of our conclusions to models with this structure. Furthermore, the example of Hilbert space fragmentation suggests that the Liouvillian spectral transition may extend beyond QMBSs to other types of weak ergodicity breaking, warranting further study. Another open question concerns other types of dissipation beyond pure dephasing and their impact on the spectral transition. Finally, in closed systems, QMBSs have been proposed for quantum sensing [60], and it would be interesting to explore the sensitivity of such applications to dephasing noise.

Acknowledgments—We thank Professors Jiasen Jin, Zheng-Wei Zhou, Wen-Ge Wang, Xiong-Jun Liu, and Dong-Lin Deng for helpful discussions. We also appreciate Dr. Jie Ren discussion on TEBD simulation for quantum open systems. This work was supported by the National Natural Science Foundation of China (Grants No. 12375021 and No. 12247101), the Zhejiang Provincial Natural Science Foundation of China (Grant No. LD25A050002), the National Key Research and Development Program of China (Grant No. No. 2022YFA1404203) and the Fundamental Research Funds for the Central Universities (Grant No. lzujbky-2024-jdzx06). Z. P. acknowledges support by the Leverhulme Trust Research Leadership Award RL-2019-015 and EPSRC Grant EP/Z533634/1. This research was supported in part by grant NSF PHY-2309135 to the Kavli Institute for Theoretical Physics (KITP).

Data availability—The data that support the findings of this article are openly available [94].

[1] I. Bloch, J. Dalibard, and S. Nascimbène, Quantum simulations with ultracold quantum gases, Nat. Phys. **8**, 267 (2012).
[2] I. M. Georgescu, S. Ashhab, and F. Nori, Quantum simulation, Rev. Mod. Phys. **86**, 153 (2014).
[3] M. Kjaergaard, M. E. Schwartz, J. Braumüller, P. Krantz, J. I.-J. Wang, S. Gustavsson, and W. D. Oliver, Superconducting qubits: Current state of play, Annu. Rev. Condens. Matter Phys. **11**, 369 (2020).
[4] A. Browaeys and T. Lahaye, Many-body physics with individually controlled Rydberg atoms, Nat. Phys. **16**, 132 (2020).
[5] C. Monroe, W. C. Campbell, L.-M. Duan, Z.-X. Gong, A. V. Gorshkov, P. W. Hess, R. Islam, K. Kim, N. M. Linke, G. Pagano, P. Richerme, C. Senko, and N. Y. Yao, Programmable quantum simulations of spin systems with trapped ions, Rev. Mod. Phys. **93**, 025001 (2021).
[6] J. M. Deutsch, Quantum statistical mechanics in a closed system, Phys. Rev. A **43**, 2046 (1991).
[7] M. Srednicki, Chaos and quantum thermalization, Phys. Rev. E **50**, 888 (1994).
[8] M. Rigol, V. Dunjko, and M. Olshanii, Thermalization and its mechanism for generic isolated quantum systems, Nature (London) **452**, 854 (2008).
[9] L. D'Alessio, Y. Kafri, A. Polkovnikov, and M. Rigol, From quantum chaos and eigenstate thermalization to statistical mechanics and thermodynamics, Adv. Phys. **65**, 239 (2016).
[10] M. Ueda, Quantum equilibration, thermalization and prethermalization in ultracold atoms, Nat. Rev. Phys. **2**, 669 (2020).
[11] M. Serbyn, D. A. Abanin, and Z. Papić, Quantum many-body scars and weak breaking of ergodicity, Nat. Phys. **17**, 675 (2021).
[12] S. Moudgalya, B. A. Bernevig, and N. Regnault, Quantum many-body scars and Hilbert space fragmentation: A review of exact results, Rep. Prog. Phys. **85**, 086501 (2022).
[13] A. Chandran, T. Iadecola, V. Khemani, and R. Moessner, Quantum many-body scars: A quasiparticle perspective, Annu. Rev. Condens. Matter Phys. **14**, 443 (2023).
[14] H. Bernien, S. Schwartz, A. Keesling, H. Levine, A. Omran, H. Pichler, S. Choi, A. S. Zibrov, M. Endres, M. Greiner *et al.*, Probing many-body dynamics on a 51-atom quantum simulator, Nature (London) **551**, 579 (2017).
[15] C. J. Turner, A. A. Michailidis, D. A. Abanin, M. Serbyn, and Z. Papić, Weak ergodicity breaking from quantum many-body scars, Nat. Phys. **14**, 745 (2018).
[16] W. W. Ho, S. Choi, H. Pichler, and M. D. Lukin, Periodic orbits, entanglement, and quantum many-body scars in

constrained models: Matrix product state approach, Phys. Rev. Lett. **122**, 040603 (2019).
[17] S. Choi, C. J. Turner, H. Pichler, W. W. Ho, A. A. Michailidis, Z. Papić, M. Serbyn, M. D. Lukin, and D. A. Abanin, Emergent SU(2) dynamics and perfect quantum many-body scars, Phys. Rev. Lett. **122**, 220603 (2019).
[18] F. M. Surace, P. P. Mazza, G. Giudici, A. Lerose, A. Gambassi, and M. Dalmonte, Lattice gauge theories and string dynamics in Rydberg atom quantum simulators, Phys. Rev. X **10**, 021041 (2020).
[19] V. Khemani, C. R. Laumann, and A. Chandran, Signatures of integrability in the dynamics of Rydberg-blockaded chains, Phys. Rev. B **99**, 161101(R) (2019).
[20] C.-J. Lin and O. I. Motrunich, Exact quantum many-body scar states in the Rydberg-blockaded atom chain, Phys. Rev. Lett. **122**, 173401 (2019).
[21] C.-J. Lin, V. Calvera, and T. H. Hsieh, Quantum many-body scar states in two-dimensional Rydberg atom arrays, Phys. Rev. B **101**, 220304(R) (2020).
[22] D. Bluvstein, A. Omran, H. Levine, A. Keesling, G. Semeghini, S. Ebadi, T. T. Wang, A. A. Michailidis, N. Maskara, W. W. Ho, S. Choi, M. Serbyn, M. Greiner, V. Vuletić, and M. D. Lukin, Controlling quantum many-body dynamics in driven Rydberg atom arrays, Science **371**, 1355 (2021).
[23] I. Mondragon-Shem, M. G. Vavilov, and I. Martin, Fate of quantum many-body scars in the presence of disorder, PRX Quantum **2**, 030349 (2021).
[24] K. Omiya and M. Müller, Quantum many-body scars in bipartite Rydberg arrays originating from hidden projector embedding, Phys. Rev. A **107**, 023318 (2023).
[25] L. Zhao, P. R. Datla, W. Tian, M. M. Aliyu, and H. Loh, Observation of quantum thermalization restricted to Hilbert space fragments and $\mathbb{Z}_{2k}$ scars, Phys. Rev. X **15**, 011035 (2025).
[26] A. Kerschbaumer, M. Ljubotina, M. Serbyn, and J.-Y. Desaules, Quantum many-body scars beyond the PXP model in Rydberg simulators, Phys. Rev. Lett. **134**, 160401 (2025).
[27] D. Ding, Z. Bai, Z. Liu, B. Shi, G. Guo, W. Li, and C. S. Adams, Ergodicity breaking from Rydberg clusters in a driven-dissipative many-body system, Sci. Adv. **10**, eadl5893 (2024).
[28] A. N. Ivanov and O. I. Motrunich, Many exact area-law scar eigenstates in the nonintegrable PXP and related models, arXiv:2503.16327.
[29] S. Moudgalya, N. Regnault, and B. A. Bernevig, Entanglement of exact excited states of Affleck-Kennedy-Lieb-Tasaki models: Exact results, many-body scars, and violation of the strong eigenstate thermalization hypothesis, Phys. Rev. B **98**, 235156 (2018).
[30] M. Schecter and T. Iadecola, Weak ergodicity breaking and quantum many-body scars in spin-1 XY magnets, Phys. Rev. Lett. **123**, 147201 (2019).
[31] K. Yang, Y. Zhang, K.-Y. Li, K.-Y. Lin, S. Gopalakrishnan, M. Rigol, and B. L. Lev, Phantom energy in the nonlinear response of a quantum many-body scar state, Science **385**, 1063 (2024).
[32] Z. Guo, B. Liu, Y. Gao, A. Yang, J. Wang, J. Ma, and L. Ying, Origin of Hilbert-space quantum scars in unconstrained models, Phys. Rev. B **108**, 075124 (2023).
[33] A. Hudomal, I. Vasić, N. Regnault, and Z. Papić, Quantum scars of bosons with correlated hopping, Commun. Phys. **3**, 99 (2020).
[34] H. Zhao, J. Vovrosh, F. Mintert, and J. Knolle, Quantum many-body scars in optical lattices, Phys. Rev. Lett. **124**, 160604 (2020).
[35] J.-Y. Desaules, A. Hudomal, C. J. Turner, and Z. Papić, Proposal for realizing quantum scars in the tilted 1D Fermi-Hubbard model, Phys. Rev. Lett. **126**, 210601 (2021).
[36] S. Scherg, T. Kohlert, P. Sala, F. Pollmann, B. Hebbe Madhusudhana, I. Bloch, and M. Aidelsburger, Observing non-ergodicity due to kinetic constraints in tilted Fermi-Hubbard chains, Nat. Commun. **12**, 4490 (2021).
[37] G.-X. Su, H. Sun, A. Hudomal, J.-Y. Desaules, Z.-Y. Zhou, B. Yang, J. C. Halimeh, Z.-S. Yuan, Z. Papić, and J.-W. Pan, Observation of many-body scarring in a Bose-Hubbard quantum simulator, Phys. Rev. Res. **5**, 023010 (2023).
[38] D. Adler, D. Wei, M. Will, K. Srakaew, S. Agrawal, P. Weckesser, R. Moessner, F. Pollmann, I. Bloch, and J. Zeiher, Observation of Hilbert space fragmentation and fractonic excitations in 2D, Nature (London) **636**, 80 (2024).
[39] P. Zhang, H. Dong, Y. Gao, L. Zhao, J. Hao, J.-Y. Desaules, Q. Guo, J. Chen, J. Deng, B. Liu *et al.*, Many-body Hilbert space scarring on a superconducting processor, Nat. Phys. **19**, 120 (2023).
[40] P. G. Larsen, A. E. B. Nielsen, A. Eckardt, and F. Petiziol, Experimental protocol for observing single quantum many-body scars with transmon qubits, arXiv:2410.14613.
[41] N. Shiraishi and T. Mori, Systematic construction of counterexamples to the eigenstate thermalization hypothesis, Phys. Rev. Lett. **119**, 030601 (2017).
[42] S. Ok, K. Choo, C. Mudry, C. Castelnovo, C. Chamon, and T. Neupert, Topological many-body scar states in dimensions one, two, and three, Phys. Rev. Res. **1**, 033144 (2019).
[43] N. Shibata, N. Yoshioka, and H. Katsura, Onsager's scars in disordered spin chains, Phys. Rev. Lett. **124**, 180604 (2020).
[44] P. A. McClarty, M. Haque, A. Sen, and J. Richter, Disorder-free localization and many-body quantum scars from magnetic frustration, Phys. Rev. B **102**, 224303 (2020).
[45] K. Lee, R. Melendrez, A. Pal, and H. J. Changlani, Exact three-colored quantum scars from geometric frustration, Phys. Rev. B **101**, 241111(R) (2020).
[46] K. Pakrouski, P. N. Pallegar, F. K. Popov, and I. R. Klebanov, Many-body scars as a group invariant sector of Hilbert space, Phys. Rev. Lett. **125**, 230602 (2020).
[47] D. K. Mark and O. I. Motrunich, η-pairing states as true scars in an extended Hubbard model, Phys. Rev. B **102**, 075132 (2020).
[48] J. Ren, C. Liang, and C. Fang, Quasisymmetry groups and many-body scar dynamics, Phys. Rev. Lett. **126**, 120604 (2021).
[49] S. Mohapatra and A. C. Balram, Pronounced quantum many-body scars in the one-dimensional spin-1 Kitaev model, Phys. Rev. B **107**, 235121 (2023).
[50] P. Kolb and K. Pakrouski, Stability of the many-body scars in fermionic spin-1/2 models, PRX Quantum **4**, 040348 (2023).

[51] N. S. Srivatsa, H. Yarloo, R. Moessner, and A. E. B. Nielsen, Mobility edges through inverted quantum many-body scarring, Phys. Rev. B **108**, L100202 (2023).

[52] J.-Y. Desaules, D. Banerjee, A. Hudomal, Z. Papić, A. Sen, and J. C. Halimeh, Weak ergodicity breaking in the Schwinger model, Phys. Rev. B **107**, L201105 (2023).

[53] J. C. Halimeh, L. Barbiero, P. Hauke, F. Grusdt, and A. Bohrdt, Robust quantum many-body scars in lattice gauge theories, Quantum **7**, 1004 (2023).

[54] B. Buča, Unified theory of local quantum many-body dynamics: Eigenoperator thermalization theorems, Phys. Rev. X **13**, 031013 (2023).

[55] L. Gotta, S. Moudgalya, and L. Mazza, Asymptotic quantum many-body scars, Phys. Rev. Lett. **131**, 190401 (2023).

[56] S. Moudgalya and O. I. Motrunich, Exhaustive characterization of quantum many-body scars using commutant algebras, Phys. Rev. X **14**, 041069 (2024).

[57] B. Evrard, A. Pizzi, S. I. Mistakidis, and C. B. Dag, Quantum scars and regular eigenstates in a chaotic spinor condensate, Phys. Rev. Lett. **132**, 020401 (2024).

[58] L. Logarić, S. Dooley, S. Pappalardi, and J. Goold, Quantum many-body scars in dual-unitary circuits, Phys. Rev. Lett. **132**, 010401 (2024).

[59] A. Pizzi, B. Evrard, C. B. Dag, and J. Knolle, Quantum scars in many-body systems, Nat. Commun. **16**, 6722 (2025).

[60] S. Dooley, Robust quantum sensing in strongly interacting systems with many-body scars, PRX Quantum **2**, 020330 (2021).

[61] J.-Y. Desaules, F. Pietracaprina, Z. Papić, J. Goold, and S. Pappalardi, Extensive multipartite entanglement from SU(2) quantum many-body scars, Phys. Rev. Lett. **129**, 020601 (2022).

[62] S. Dooley, S. Pappalardi, and J. Goold, Entanglement enhanced metrology with quantum many-body scars, Phys. Rev. B **107**, 035123 (2023).

[63] A. Omran, H. Levine, A. Keesling, G. Semeghini, T. T. Wang, S. Ebadi, H. Bernien, A. S. Zibrov, H. Pichler, S. Choi, J. Cui, M. Rossignolo, P. Rembold, S. Montangero, T. Calarco, M. Endres, M. Greiner, V. Vuletić, and M. D. Lukin, Generation and manipulation of Schrödinger cat states in Rydberg atom arrays, Science **365**, 570 (2019).

[64] T. Albash and D. A. Lidar, Decoherence in adiabatic quantum computation, Phys. Rev. A **91**, 062320 (2015).

[65] Y. Yao *et al.*, Observation of many-body Fock space dynamics in two dimensions, Nat. Phys. **19**, 1459 (2023).

[66] B. Olmos, I. Lesanovsky, and J. P. Garrahan, Facilitated spin models of dissipative quantum glasses, Phys. Rev. Lett. **109**, 020403 (2012).

[67] K. Macieszczak, M. Guţă, I. Lesanovsky, and J. P. Garrahan, Towards a theory of metastability in open quantum dynamics, Phys. Rev. Lett. **116**, 240404 (2016).

[68] B. Buča, J. Tindall, and D. Jaksch, Non-stationary coherent quantum many-body dynamics through dissipation, Nat. Commun. **10**, 1730 (2019).

[69] C. Booker, B. Buča, and D. Jaksch, Non-stationarity and dissipative time crystals: Spectral properties and finite-size effects, New J. Phys. **22**, 085007 (2020).

[70] F. M. Gambetta, F. Carollo, M. Marcuzzi, J. P. Garrahan, and I. Lesanovsky, Discrete time crystals in the absence of manifest symmetries or disorder in open quantum systems, Phys. Rev. Lett. **122**, 015701 (2019).

[71] H. Keßler, P. Kongkhambut, C. Georges, L. Mathey, J. G. Cosme, and A. Hemmerich, Observation of a dissipative time crystal, Phys. Rev. Lett. **127**, 043602 (2021).

[72] H.-R. Wang, D. Yuan, S.-Y. Zhang, Z. Wang, D.-L. Deng, and L.-M. Duan, Embedding quantum many-body scars into decoherence-free subspaces, Phys. Rev. Lett. **132**, 150401 (2024).

[73] X.-P. Jiang, M. Xu, X. Yang, H. Hou, Y. Wang, and L. Pan, Robustness of quantum many-body scars in the presence of Markovian bath, arXiv:2501.00886.

[74] A. M. García-García, Z. Lu, L. Sá, and J. J. M. Verbaarschot, Lindblad many-body scars, arXiv:2503.06665.

[75] C.-J. Lin, A. Chandran, and O. I. Motrunich, Slow thermalization of exact quantum many-body scar states under perturbations, Phys. Rev. Res. **2**, 033044 (2020).

[76] F. M. Surace, M. Votto, E. G. Lazo, A. Silva, M. Dalmonte, and G. Giudici, Exact many-body scars and their stability in constrained quantum chains, Phys. Rev. B **103**, 104302 (2021).

[77] S. Moudgalya, N. Regnault, and B. A. Bernevig, η-pairing in Hubbard models: From spectrum generating algebras to quantum many-body scars, Phys. Rev. B **102**, 085140 (2020).

[78] D. K. Mark, C.-J. Lin, and O. I. Motrunich, Unified structure for exact towers of scar states in the Affleck-Kennedy-Lieb-Tasaki and other models, Phys. Rev. B **101**, 195131 (2020).

[79] N. O'Dea, F. Burnell, A. Chandran, and V. Khemani, From tunnels to towers: Quantum scars from Lie algebras and q-deformed Lie algebras, Phys. Rev. Res. **2**, 043305 (2020).

[80] K. Bull, J.-Y. Desaules, and Z. Papić, Quantum scars as embeddings of weakly broken Lie algebra representations, Phys. Rev. B **101**, 165139 (2020).

[81] H. Dong, J.-Y. Desaules, Y. Gao, N. Wang, Z. Guo, J. Chen, Y. Zou, F. Jin, X. Zhu, P. Zhang, H. Li, Z. Wang, Q. Guo, J. Zhang, L. Ying, and Z. Papić, Disorder-tunable entanglement at infinite temperature, Sci. Adv. **9**, eadj3822 (2023).

[82] T. Prosen, $\mathbb{PT}$-symmetric quantum Liouvillean dynamics, Phys. Rev. Lett. **109**, 090404 (2012).

[83] Q. Chen, S. A. Chen, and Z. Zhu, Weak ergodicity breaking in non-Hermitian many-body systems, SciPost Phys. **15**, 052 (2023).

[84] R. Shen, F. Qin, J.-Y. Desaules, Z. Papić, and C. H. Lee, Enhanced many-body quantum scars from the non-Hermitian Fock skin effect, Phys. Rev. Lett. **133**, 216601 (2024).

[85] T. Iadecola and M. Žnidarič, Exact localized and ballistic eigenstates in disordered chaotic spin ladders and the Fermi-Hubbard model, Phys. Rev. Lett. **123**, 036403 (2019).

[86] See Supplemental Material at http://link.aps.org/supplemental/10.1103/4my3-vk6c for details of the derivations and results for other models.

[87] H.-P. Breuer and F. Petruccione, *The Theory of Open Quantum Systems* (Oxford University Press, USA, 2002).

[88] M. Fishman, S. R. White, and E. M. Stoudenmire, The ITensor software library for tensor network calculations, SciPost Phys. Codebases 4 (2022).

[89] L. Sá, P. Ribeiro, and T. c. v. Prosen, Symmetry classification of many-body Lindbladians: Tenfold way and beyond, Phys. Rev. X **13**, 031019 (2023).

[90] J.-Y. Desaules, E. J. Gustafson, A. C. Y. Li, Z. Papić, and J. C. Halimeh, Robust finite-temperature many-body scarring on a quantum computer, Phys. Rev. A **110**, 042606 (2024).

[91] P. Jurcevic and L. C. Govia, Effective qubit dephasing induced by spectator-qubit relaxation, Quantum Sci. Technol. **7**, 045033 (2022).

[92] H. Levine, A. Keesling, A. Omran, H. Bernien, S. Schwartz, A. S. Zibrov, M. Endres, M. Greiner, V. Vuletić, and M. D. Lukin, High-fidelity control and entanglement of Rydberg-atom qubits, Phys. Rev. Lett. **121**, 123603 (2018).

[93] D. Hahn, P. A. McClarty, and D. J. Luitz, Information dynamics in a model with Hilbert space fragmentation, SciPost Phys. **11**, 074 (2021).

[94] Jin-Lou Ma, Zexian Guo, Yu Gao, Zlatko Papić, and Lei Ying, Version v1, Zenodo, https://doi.org/10.5281/zenodo.17302575 (2025).

[95] P. Fendley, K. Sengupta, and S. Sachdev, Competing density-wave orders in a one-dimensional hard-boson model, Phys. Rev. B **69**, 075106 (2004).

[96] I. Lesanovsky and H. Katsura, Interacting Fibonacci anyons in a Rydberg gas, Phys. Rev. A **86**, 041601(R) (2012).

[97] C. J. Turner, A. A. Michailidis, D. A. Abanin, M. Serbyn, and Z. Papić, Quantum scarred eigenstates in a Rydberg atom chain: Entanglement, breakdown of thermalization, and stability to perturbations, Phys. Rev. B **98**, 155134 (2018).

[98] K. Omiya and M. Müller, Fractionalization paves the way to local projector embeddings of quantum many-body scars, Phys. Rev. B **108**, 054412 (2023).

End Matter

Transition in the PXP model—Another paradigmatic model of QMBSs is the PXP model describing Rydberg atom arrays [14]. The PXP Hamiltonian is [95,96]

$$\hat{H} = \hat{H}_{\rm PXP} = \Omega \sum_{j}^{L} \hat{P}_{j-1}\hat{\sigma}_j^x \hat{P}_{j+1}, \quad \hat{P}_j = (1-\hat{\sigma}_j^z)/2, \tag{A1}$$

where $\hat{\sigma}_j^{x,y,z}$ are the Pauli matrices and we set the Rabi frequency to $\Omega = 1$. We impose periodic boundary conditions, with $L+1 \equiv 1$. The PXP model features revival dynamics when the system is quenched from the initial state $|\mathbb{Z}_2\rangle \equiv |\uparrow\downarrow\uparrow\downarrow\cdots\rangle$ [15,97]. Below we demonstrate that the PXP model with pure dephasing exhibits similar behavior to the CL model.

PXP spectral transition—Figures 4(a) and 4(b) illustrate the Liouvillian spectra for the PXP model for two dephasing rates. These results are qualitatively similar to the CL model in Fig. 1: for weak dephasing $\gamma = 0.0004$, the QMBS eigenvalues cluster around $\mathrm{Re}(\lambda') = 0$, while at larger dephasing, $\gamma = 0.04$, these eigenvalues pair-wisely shift along the real axis. The main difference with Fig. 1 is that the PXP model does not possess the $\mathcal{T}_-$ superoperator obeying $\mathcal{T}_-\mathcal{L}\mathcal{T}_-^{-1} = -\mathcal{L}$ [89]. Hence, its Liouvillian spectrum, even at small $\gamma = 0.0004$, is not confined to the real- and imaginary axes and LPTS is already broken at that point, even for QMBS eigenvalues. However, the scar eigenvalues cluster around the axes at small γ and exhibit similar movement under dephasing as in the CL model. We next show that scar eigenvalues of the PXP Liouvillian indeed undergo sharp jumps upon sweeping the dephasing rate, similar to the CL model.

Figure 4(c) illustrates the imaginary part of eigenvalues and real part of normalized eigenvalues λ'/γ as a function of γ. Several eigenvalues with momentum $q = 0$ remain stationary at weak dephasing, while some pairs of eigenvalues abruptly bifurcate into two branches around specific dephasing rates $\gamma_\star^{(1,2\ldots)}$. In contrast, no such bifurcations occur in the momentum sector $q = \pi$, mirroring the behavior of the CL model with respect to inversion symmetry in Fig. 2. The QMBS eigenmodes are remarkable for their large overlap with $|\rho_{\mathbb{Z}_2}\rangle\!\rangle = |\mathbb{Z}_2\rangle \otimes |\mathbb{Z}_2\rangle$.

Upon closer inspection of Fig. 4(c), we see that the process of eigenvalue bifurcation is smoother compared to the CL model in Fig. 2(a). This can be understood in the framework of perturbation theory $\mathcal{L}_S \approx \mathcal{S}_0 + \mathcal{E} + \gamma_{\rm eff}\mathcal{D}'$, suitably extended to the PXP model where the QMBS Hamiltonian $\hat{S}_0$ and the self-energy $\hat{\Sigma}$ are expressed in a dimerized spin-1 basis [24,98]. The dissipator $\mathcal{D}' = \sum_j \hat{\sigma}_j^z \otimes \hat{\sigma}_j^z$ splits into a linear and quadratic term upon mapping to the dimerized spin-1 basis; see SM [86]. When only the linear term is considered, the spectrum exhibits $\mathbb{PT}$ symmetry and spectral transition. However, when both linear and quadratic term are included, the $\mathcal{T}_-$ symmetry is no longer present but we capture the rounded profile of the spectral evolution curves. The perturbative estimate, including both linear and quadratic terms, is plotted in Fig. 4(c) and shows good agreement with the numerics.

The typical Liouvillian spectral transition point $\bar{\gamma}_\star^{\rm S}$ for the PXP scar eigenmodes can be estimated from the spacings $\bar{\delta}$ of nondegenerate scar eigenvalues at $\gamma = 0$ according to the same expression, $\bar{\gamma}_\star^{\rm S} \sim \bar{\delta}\|\mathcal{D}'\|^{-1}$, used previously for the CL model in the main text. As confirmed in Fig. 4(e), $\bar{\delta} \sim LD^{-2}$ for thermal eigenvalues, while the scar $\bar{\delta}$ is nearly independent of D. Thus, the typical critical point for PXP scar eigenmodes also scales as $\bar{\gamma}_\star^{\rm S} \sim L^{-1}$, consistent with the approximate scars in the CL model. This is also confirmed by the perturbation theory result in Fig. 4(d), where we keep only the linear term of the

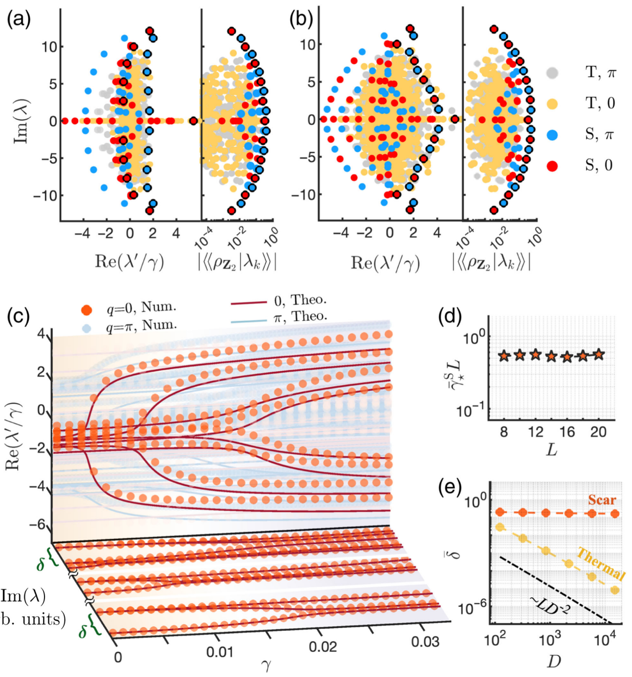

FIG. 4. (a),(b) The Liouvillian eigenspectra of the PXP model for dephasing strengths $\gamma = 0.0004$ and $\gamma = 0.04$. Red and blue dots represent scar (S) eigenvalues, while yellow and gray ones represent thermal (T) eigenvalues. These are further classified by momenta $q = 0$ and π under translations. The right panels in (a),(b) show the overlaps of Liouvillian eigenmodes with $|\rho_{Z_2}\rangle\rangle$, with black open circles highlighting local maxima. (c) The evolution of the Liouvillian spectrum, $\mathrm{Im}(\lambda)$ and $\mathrm{Re}(\lambda'/\gamma)$, as the dephasing rate γ is varied. For improved visualization, the imaginary values in panel (c) have been shifted within a small window. The curves are results of perturbation theory, following Eq. (5) [86]. (d) The average spectral transition point $\bar{\gamma}_\star^S L$ as a function of system size L obtained in perturbation theory. (e) The average scar eigenvalue spacing $\bar{\delta}$, at zero dephasing, plotted as a function of the corresponding sector dimension D. Data in panels (a)–(c) is obtained by exact diagonalization of the PXP model for a system size of $L = 10$ with periodic boundary conditions.

dissipator, allowing to unambiguously identify the spectral transition points and their mean value.

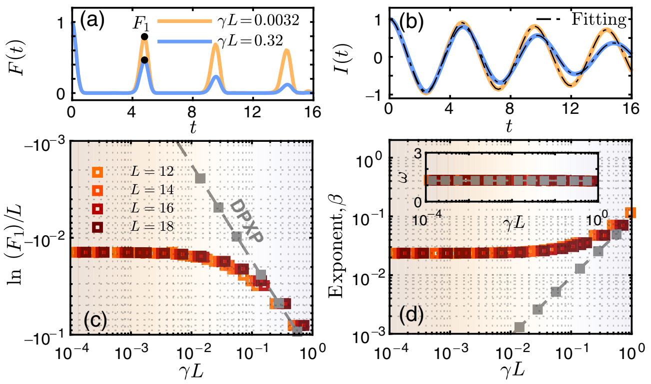

FIG. 5. The dynamics of the global fidelity $F(t)$ (a) and imbalance $I(t)$ (b) in the PXP model for two dephasing rates at system size $L = 16$. The black circles in (a) denote the first fidelity revival peak, F_1, while the black dash-dotted lines in (b) are fits of the imbalance dynamics to $\bar{I}(t)$. (c) The global fidelity density at the first revival, $\ln(F_1)/L$ and (d) the decay coefficient β of density imbalance for the PXP model as a function of dephasing γ. Parameters (β, ω) are obtained by fitting the imbalance dynamics over the time period [0, 5]. These results are obtained by exact diagonalization.

Finally, similar to the CL model in the main text, we check for the robustness of scar signatures in the dynamics by performing time evolution generated by the Lindblad equation for the PXP model with pure dephasing. Here we take as initial state $|\rho_{Z_2}\rangle\rangle$ and the resulting fidelity density at the first revival, $\ln F_1/L$, as well as the imbalance decay β and frequency ω, are shown in Fig. 5. These results mirror those for the CL model, in particular β has a similarly weak dependence on γL as long as $\gamma < \bar{\gamma}_\star^{\mathrm{S}}$.

To confirm that these results are due to approximate scars, we consider a deformation of the PXP model [17,19,80] for which QMBSs assume a nearly exact form:

$$\hat{H}_{\mathrm{DPXP}} = \hat{H}_{\mathrm{PXP}} + \sum_{j}^{L}\sum_{d=2}^{L/2} J_{\mathrm{d}} \hat{P}_{j-1}\hat{\sigma}_j^x \hat{P}_{j+1}(\hat{\sigma}_{j-d}^z + \hat{\sigma}_{j+d}^z). \tag{B1}$$

At the optimal coupling strength $J_{\mathrm{d}} = 0.051(\phi^{d-1} + \phi^{1-d})^{-2}$, with $\phi = (1 + \sqrt{5})/2$, the scar subspace contains $L + 1$ eigenstates that are almost perfectly decoupled from the thermal bulk of the spectrum [17]. This DPXP model indeed behaves similarly to the exact scars in the CL model with $J_{\mathrm{x},j} = 0$, e.g., the imbalance decay coefficient β exhibits a similar power-law dependence on γ in both cases. The similarity extends to the Liouvillian spectra, as the DPXP model also exhibits a spectral transition for infinitesimal γ [86].